Optical Engineering

OpticalEngineering.SPIEDigitalLibrary.org

Path planning and parameter optimization of uniform removal in active feed polishing

Jian Liu
Shaozhi Wang
Chunlei Zhang
Linghua Zhang
Huanan Chen

SPIE.

Optical Engineering 54(6), 065101 (June 2015)

Path planning and parameter optimization of uniform removal in active feed polishing

Jian Liu,* Shaozhi Wang, Chunlei Zhang, Linghua Zhang, and Huanan Chen
Chinese Academy of Science, Changchun Institute of Optics, Fine Mechanics and Physics,
Engineering Research Center of Extreme Precision Optics, State Key Laboratory of Applied Optics,
Changchun 130033, China

Abstract. A high-quality ultrasmooth surface is demanded in short-wave optical systems. However, the existing polishing methods have difficulties meeting the requirement on spherical or aspheric surfaces. As a new kind of small tool polishing method, active feed polishing (AFP) could attain a surface roughness of less than 0.3 nm (RMS) on spherical elements, although AFP may magnify the residual figure error or mid-frequency error. The purpose of this work is to propose an effective algorithm to realize uniform removal of the surface in the processing. At first, the principle of the AFP and the mechanism of the polishing machine are introduced. In order to maintain the processed figure error, a variable pitch spiral path planning algorithm and the dwell time-solving model are proposed. For suppressing the possible mid-frequency error, the uniformity of the synthesis tool path, which is generated by an arbitrary point at the polishing tool bottom, is analyzed and evaluated, and the angular velocity ratio of the tool spinning motion to the revolution motion is optimized. Finally, an experiment is conducted on a convex spherical surface and an ultrasmooth surface is finally acquired. In conclusion, a high-quality ultrasmooth surface can be successfully obtained with little degradation of the figure and mid-frequency errors by the algorithm. [DOI: 10.1117/1.OE.54.6.065101]

Keywords: ultrasmooth polishing; uniform removal; path planning; parameter optimization.

Paper 141363 received Sep. 3, 2014; accepted for publication May 7, 2015; published online Jun. 4, 2015.

1 Introduction

With the development of optoelectronic technology, the short-wave optical system has introduced higher and higher requirements on the surface quality of optical elements. The ultrasmooth surface polishing technology has gradually become an important research direction.[1] At present, the methods that can obtain an ultrasmooth surface mainly includes the float polishing (FP),[2,3] the elastic emission machining,[4–6] the bowl polishing,[7] the chemical machining polishing,[8,9] and so on. One part of these methods can only be used for flat surfaces, and the others are not suitable for mass production.

In order to realize the ultrasmooth polishing of a spherical surface, especially an aspheric surface, we have developed the active feed polishing (AFP),[10] which combines the advantages of the small tool polishing[11] and the FP[12] and we also developed a five axes linkage computer numerical control (CNC) machine to realize the AFP. The target of this process is to acquire an ultrasmooth surface of less than 0.3 nm RMS roughness, while maintaining the figure error and suppressing the mid-frequency error. Thus, the purpose of this paper is to propose some algorithm to realize the uniform removal on full aperture.

In this paper, the principle of the AFP and the machine motion mechanism are first introduced. Then a variable pitch spiral path planning algorithm together with a dwell time-solving model is proposed to realize uniform removal in the low spatial frequency range. The uniformity of the synthesis tool path, which is generated by an arbitrary point at the bottom of the polishing tool, is analyzed and evaluated. The angular velocity ratio of the tool spinning rotation to the revolution motion is also optimized to suppress mid-frequency errors. Finally, the algorithm is verified by an experiment.

2 Basic Theories

2.1 *Material Removal Theory*

The principle of the AFP technology is shown in Fig. 1. The slurry is supplied from the center of the polishing tool and flows through the microholes at the bottom. The polishing tool is rotating at high speed so that the pad is supported by a fluid layer between the pad and the workpiece.[13,14] Meanwhile, the slurry in this layer moves along the circumferential direction and the fast moving microabrasives in the slurry scratch the surface at the tangential direction and eventually remove the surface atoms of the workpiece.

Although the material removal mechanism of the AFP is based on the principle of FP, its movement is realized by the small tool polishing. Therefore, the theory of small tool polishing is also suitable for this method. In the description of small tool polishing theory, there is an important equation to describe the removal amount, which was proposed by Preston[15] and Dai et al.:

$$dz = kvpdt,$$

where dz is the unit time removal amount, k is the proportional coefficient which is related to the polishing conditions, v is the instantaneous relative velocity, and p is the

---

*Address all correspondence to: Jian Liu, E-mail: emailtoliujian@126.com

0091-3286 /2015/$25.00 © 2015 SPIE

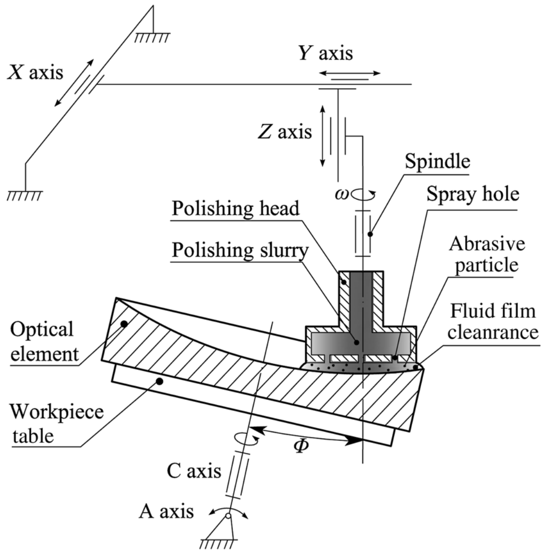

Fig. 1 Principle and mechanism of the active feed polishing.

instantaneous pressure at point (x, y). So the material removal amount at point (x, y) in time span of t is

$$z = \int_0^t k v p \, \mathrm{d}\tau. \tag{1}$$

2.2 *Surface Generation Method*

Figure 1 also illustrates the machine motion of the AFP. Based on the surface generation theory, the analytic expression, which describes the motor function of this machine, is

$$W/AC \cdot YXZ/\gamma_p/T,$$

where W is the workpiece, A is the axis rotating with the X axis, C is another axis rotating with the Z axis, symbol "·" denotes the machine body, YXZ denote linear axes arranged in the order Y-X-Z, γ_p is the spindle element, and T is the polishing tool. This machine belongs to a kind of five axes CNC machine with a dual rotary table. Two representative paths, the raster path and the spiral path, can both be realized on this machine. Comparatively, the spiral path is more suitable in this paper because the workpiece rotates together with the worktable in this mode, which can diminish the X and Y axes' travel and dynamic requirements.

3 Path Planning and Dwell Point Accurate Solution

3.1 *Variable Pitch Spiral Path Planning*

To illustrate the variable pitch spiral, the motion and the speed of the center point at the polishing tool bottom are considered. First, we give the definition of the well-known Archimedes' spiral

$$\rho = \frac{v}{\Omega}\theta,$$

where ρ and θ are the polar radius and helical angle, respectively, v is a constant and denotes the moving velocity of the point P, and Ω denotes the angular velocity of the half-line rotation around the pole. The spiral path generated by Eq. (2) is shown in Fig. 2(a).

The problem of Archimedes' spiral is that the resultant velocity V of P increases gradually when the polishing tool moves toward the lens edge. If the lens was polished under constants v and Ω, the dwell time will decrease when the polishing tool moves toward the edge. That is to say, the material removal will be reduced in these regions. On the other hand, the rotation of P is the main portion of V. So the velocity of axis C will exceed the machine limit at the central region $(\rho \to 0)$ if we keep V constant by controlling the angular velocity Ω. Similarly, the central region removal amount is larger than expected if the maximum angular velocity of axis C is limited.

So a new spiral path is needed in order to maintain the figure accuracy of the sample. Set the velocity of the point P moving along the half-line direction as Eq. (3):

$$v(\rho) = \begin{cases} v_{\text{const}} & \rho \le \rho_0 \\ \frac{\eta \xi(\rho)}{\rho} & \rho > \rho_0 \end{cases}, \tag{3}$$

where ρ_0 is a given radius and v_{const} is a given velocity which is usually set to be $\eta\xi(\rho_0)/\rho_0$ in order to keep the velocity continuous. η is a constant parameter which is related to the polishing process. $\xi(\rho)$ is the material removal function, which is constant in the uniform removal mode. If the half-line rotates around O with Ω and moves along with the velocity shown in Eq. (3), the resultant velocity of P is approximately a constant. The synthetic path is a variable pitch spiral with the pitch gradually reducing, which is shown in Fig. 2(b).

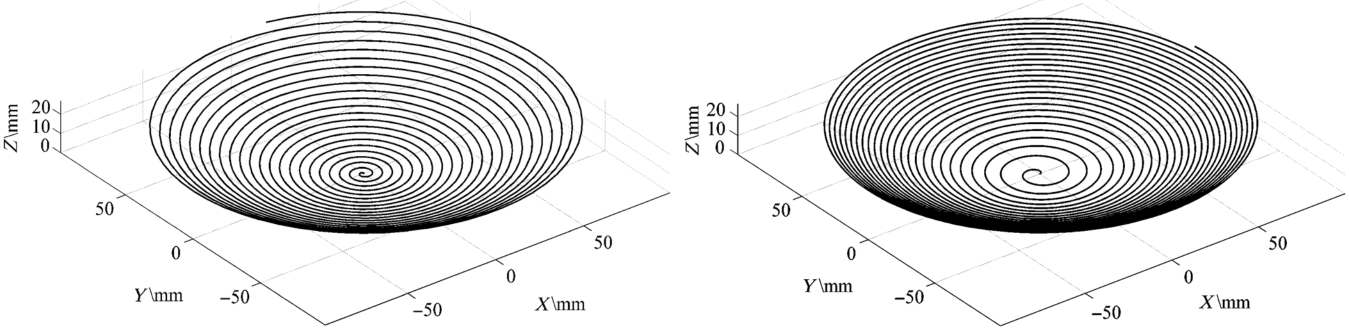

(a) (b)

Fig. 2 Spiral path: (a) moving with constant velocity and (b) moving with variable velocity.

The equation of the variable pitch spiral is shown in Eq. (4):

$$\rho = \frac{v(\rho)}{\Omega}\theta. \tag{4}$$

Equation (4) is a polar expression of the spiral path which can be applied to the planar elements. As shown in Eq. (5), a universal description of the spiral path is given in Cartesian coordinates.

$$\begin{cases} x = \frac{v(\rho)}{\Omega}\theta \cos \theta \\ y = \frac{v(\rho)}{\Omega}\theta \sin \theta \\ z = f(x, y) \end{cases}, \tag{5}$$

where $z = f(x, y)$ denotes z value of the optical surface at point (x, y).

3.2 *Exact Solution of Dwell Point*

Equation (5) just gives the analytic expression of the variable pitch spiral path. However, the path needs to be discrete and realized by a series of linear interpolations on the CNC machine. As shown in Fig. 3(a), the maximum error between linear path l and the target curve is defined as the chord error δ_t. According to the trigonometric function, the relationship among chord error, curvature radius, and microarc length can be described as follows:

$$\delta_t = R\left[1 - \cos\left(\frac{0.5L_t}{R}\right)\right],$$

where R is curvature radius of the microarc and L_t is the arc-length of the microarc. In order to accurately control the chord error δ_t of the interpolation path, an equal arc-length recursive algorithm, which solves the position and direction vector of an arbitrary point on the spiral path, is proposed here. Figure 3(b) is the schematic diagram of the algorithm.

The analytic result of θ_i is very difficult to obtain from the integral equation below:

$$\int_{\theta_{i-1}}^{\theta_i} f(x, y, \theta) = L_t,$$

thus, a numerical solution is adopted. In Fig. 3(b), O is the center of the spiral path, D_{i-1} denotes the $(i-1)$'th dwell point, θ_{i-1} is the corresponding helical angle which is the starting helical angle to calculate dwell point D_i, L_i, which satisfies $L_i \le L_t$, is the real arc length between the adjacent two dwell points, and ρ_{i-1} is the polar axis length of the current dwell point. According to the character of the spiral $\rho_{i-1} < \rho_i$, the helical angle θ_i of the dwell point D_i meets the relationship below:

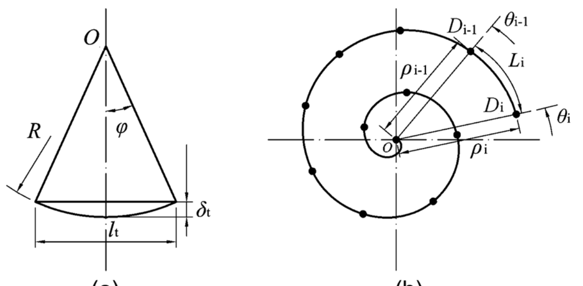

(a) (b)

Fig. 3 Schematic diagram: (a) definition of chord error and (b) solving diagram of dwell point.

$$\theta_i < \theta_{i-1} + \frac{L_t}{\rho_{i-1}}.$$

Setting L_t/ρ_{i-1} as θ^i_{step}, the search range can be given to solve the next dwell point and a discrete θ^i_{step} to an M step can be given to accurately solve $D_i(\widehat{D_{i-1}D_i} < L_t)$. M can be calculated by the following equation:

$$M = \frac{\theta^i_{\text{step}}}{\theta'_{\text{step}}} = \frac{\rho_{i-1}\theta^i_{\text{step}}}{\varepsilon},$$

where θ'_{step} is the angle discrete step $(\theta'_{\text{step}} = \varepsilon/\rho_{i-1})$, ε is the arc length discrete step, and $\varepsilon < 0.1$ mm. The solution of D_i is equal to searching the minimum n in $(0, M]$ and making Eq. (6) as follows:

$$\min_{0<n\le M}\left\{\left\{\sum_{j=1}^{n}\min\{D_{i-1} - D_j\}\right\} \ge L_t\right\}, \tag{6}$$

where $\min\{D_{i-1} - D_j\}$ denotes the nearest distance between D_{i-1} and D_j. The polar radius and helical angle of $\mathrm{D_i}$ are

$$\begin{cases} \theta_i = \theta_{i-1} + n \cdot \theta^i_{\text{step}} \\ \rho_i = \frac{v(\rho_i)}{\Omega}\theta_i \end{cases},$$

D_i can be determined according to Eq. (5). The rest can be calculated in the same manner to get the dwell point set $\{D_i, i = 1 \cdots N\}$ until ρ_i satisfies the below equation:

$$\rho_i \le 0.5 \cdot d',$$

where d' is the maximum aperture that the polishing tool center can reach; it is related to the lens aperture, the polishing tool diameter, and the bearing percentage at edge.

3.3 *Realization of Processing Path*

The center point at the polishing tool bottom is considered in the path planning algorithm in Sec. 3.1. The practical resultant velocity is not as simple as Eq. (2), because the radius r_0 of the polishing tool is not zero. The relative motion between the polishing tool and workpiece is a planetary motion whose eccentricity $e = r/\rho$ is variable. Here, the spiral motion corresponding to the center point at the polishing tool bottom is a revolution motion with angle velocity Ω and radius ρ (variable), and the tool motion is the spinning rotation with the angle velocity ω. The principle of the synthetic velocity at an arbitrary point P at the bottom of the polishing tool is shown in Fig. 4.

In Fig. 4, O_1 is the center of the spiral path and O_2 is the center at the polishing tool bottom. P is an arbitrary point on the polishing tool and the distance between P and O_2 is r. The distance between P and O_1 is r'. The velocity of P is

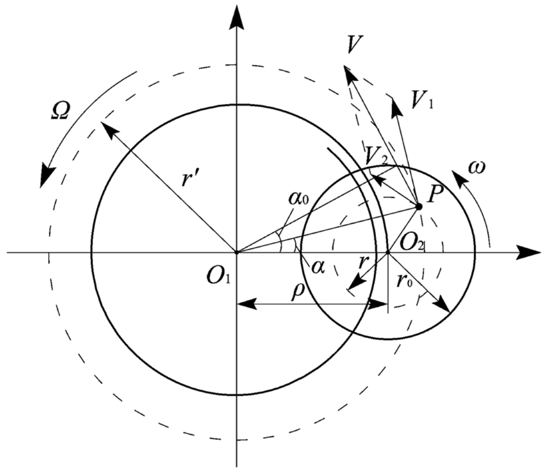

Fig. 4 Velocity diagram.

$$v(r',\alpha) = \sqrt{(\omega^2+\Omega^2)r'^2+\rho^2\Omega^2+2r'^2\omega\Omega-2\rho r'(\Omega^2+\omega\Omega)\cos\alpha}.$$

According to Eq. (1), the removal function at this dwell point is[16,17]

$$R(r',\alpha) = \lim_{t\to\infty}\left[\frac{kp}{t}\int_0^t v(r',\alpha,\tau)\mathrm{d}\tau\right].$$

This can be changed in polar form to

$$R(r') = \frac{kp}{2\pi\omega}\int_{-\alpha_0}^{\alpha_0} v(\alpha,r')\mathrm{d}\alpha,$$

where

$$\alpha_0 = \cos^{-1}\left(\frac{r'^2+\rho^2-r_0^2}{2r'\rho}\right).$$

The removal curves of different points are shown in Fig. 5.

Figure 5 shows that the removal functions are different when the polishing pad is moving to different points. Therefore, the dwell times at these points should all be calculated and the feed rate should be corrected in order to realize the uniform removal on full aperture. $R_i(r')$ denotes the removal rate when the polishing tool dwells at D_i, which can be written into matrix type $R_i = [R_{1i}\ \dots\ R_{Mi}]'$, $i = 1\dots N$, in which N is the number of dwell points and M is the number of calculation points. Set the dwell time vector to be $T = [t_1\quad\dots\quad t_i]'$ and the removal rate vector is $H = [h_1\quad\dots\quad h_i]'$. Their relationship can be described in Eq. (7):

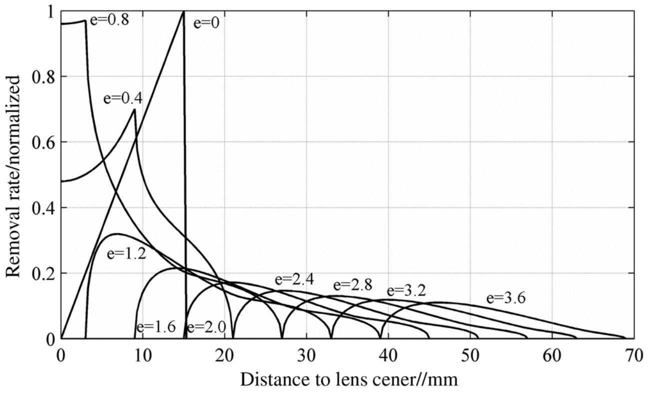

Fig. 5 Removal rate distribution.

$$\begin{bmatrix} h_1 \\ \vdots \\ h_\mathrm{M} \end{bmatrix} = [R_{1i}\quad\dots\quad R_{Mi}]\begin{bmatrix} t_1 \\ \vdots \\ t_N \end{bmatrix}. \tag{7}$$

Equation (7) could be written into a matrix equation $H = RT$. There is usually no exact solution of this equation, so the approximate solution, which minimizes the RMS value of the residual error $E = H - RT$, will be used. This problem could be described as the least squares optimization problems with non-negative constraints:[17,18]

$$\begin{cases} \min\|H-RT\| \\ T \ge 0 \end{cases}. \tag{8}$$

The target material removal rate H is constant in the uniform removal mode. The dwell time matrix T could be calculated by the least squares algorithm.[19] Finally, the polishing tool feed rate F can be calculated from Eq. (9):

$$F = \begin{cases} v_\mathrm{const} & t=0 \\ \frac{L_i}{t_i} & t>0 \end{cases}. \tag{9}$$

4 Optimization of Technology Parameters

4.1 *Calculation of Synthetic Path*

The dwell points $\{D_i, i = 1\ \cdots\ N\}$ describe the moving path of O_2. The point P, whose distance is r' from O_2, is also taken as the point of interest in order to analyze the uniformity of the removal of a single point (base on uniform removal theory).[20–23] Figure 6 shows the schematic diagram

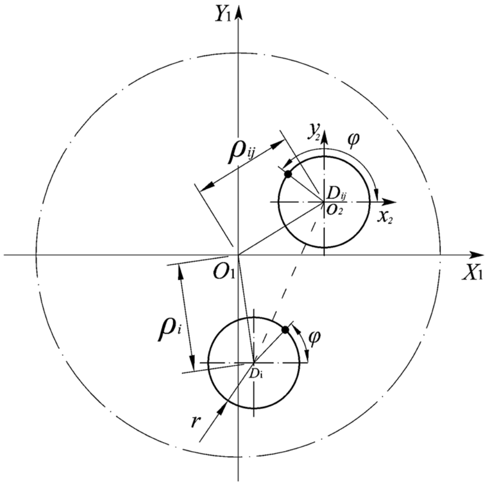

Fig. 6 Path synthesis diagram.

of the synthesizing path, where $X_1O_1Y_1$ is the global coordinate system and $x_2o_2y_2$ is the local coordinate system.

Assume that O_2 is the position of the point D_i in the revolution motion at moment t. The polar radius of this point is ρ_i and the helix angle is θ_i. The next adjacent point is D_{i+1} whose polar radius is ρ_{i+1}. According to the algorithm in Sec. 3.3, the time interval between the two points is t_i, which is further divided into S segments ($S \geq 1$, increasing S will improve the precision of the synthetic path). Then each time interval is

$$\tau = \frac{t_i}{S}.$$

The corresponding differential polar radius $\Delta\rho$ can be defined as follows:

$$\Delta\rho = \frac{\rho_{i+1} - \rho_i}{S}.$$

The rotation angle of the point P is assumed to be $\varphi = \varphi_0 + \omega t$ (where φ_0 is the initial phase angle). When the polishing tool center moves to D_{ij} after τ, the polar radius of this point is $\rho_{ij} = \rho_i + \Delta\rho j$, and the helix angle is $\theta_{ij} = \theta_i + \Omega(t + \tau j)$, $(j = 0 \cdots S - 1)$. The position of the polishing tool center can be described in a global coordinate system as

$$\begin{cases} X = \rho_{ij} \cos[\theta_i + \Omega(t + \tau j)] \\ Y = \rho_{ij} \sin[\theta_i + \Omega(t + \tau j)] \\ Z = f(X, Y) \end{cases}.$$

The rotation angle of the point P is $\varphi = \varphi_0 + \omega(t + \tau j)$. In the local coordinate system, the coordinates of the point P are described as follows:

$$\begin{cases} x = r \cos[\varphi_0 + \omega(t + \tau j)] \\ y = r \sin[\varphi_0 + \omega(t + \tau j)] \end{cases}.$$

Furthermore, according to the principle of the coordinate transformation, point P can be described in the global coordinate system as in Eq. (10):

$$\begin{cases} x' = \rho_{ij} \cos[\theta_i + \Omega(t + \tau j)] + r \cos[\varphi_0 + \omega(t + \tau j)] \\ y' = \rho_{ij} \sin[\theta_i + \Omega(t + \tau j)] + r \sin[\varphi_0 + \omega(t + \tau j)] \\ z' = f(x', y') \end{cases}. \tag{10}$$

The synthesis path between D_i and D_{i+1} can be calculated when $j = S$ according to the equation above and the rest can be done in the same manner until $i = N$. The generated synthesis path is shown in Fig. 7.

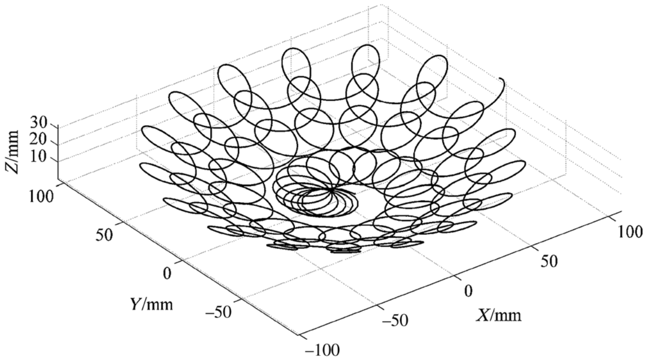

Fig. 7 Synthesis path of an arbitrary point ($r = 15$ mm, $\Omega = 15$ rpm, $\omega = 240$ rpm).

4.2 *Uniform Evaluation of Material Removal*

It is obvious that the synthesis path of an arbitrary point at the polishing tool bottom shows a periodic overlap section and the overlapped amounts of each section are unequal. This kind of periodic overlap section will cause microscopic nonuniform material removal and eventually produce a mid-frequency error. In order to evaluate the mid-frequency error induced by the path, the degree of the path overlapping should be evaluated quantitatively. Points of the synthesis path are mapped on a matrix grid and the occupancy times are recorded, which represent the times of path overlap at the grid node. The grid position that corresponds to the point $P(x, y)$ of the synthesis path could be calculated from Eq. (11):

$$\begin{cases} m = \text{ftoint}\left(\frac{x+0.5d'}{\zeta}\right) \\ n = \text{ftoint}\left(\frac{y+0.5d'}{\zeta}\right) \end{cases}, \tag{11}$$

in which m, n is the grid position, ftoint is is a rounding function, and ζ is the grid step. The accumulation topography that expresses the overlapping times of different positions is shown in Fig. 8. In the figure, AVER and RMS denote

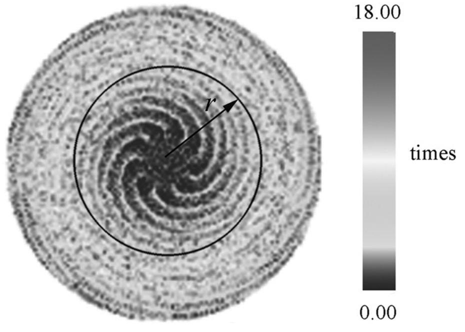

AVER=5.516 times RMS=2.90 times

Fig. 8 The accumulation figure texture of the synthesis path.

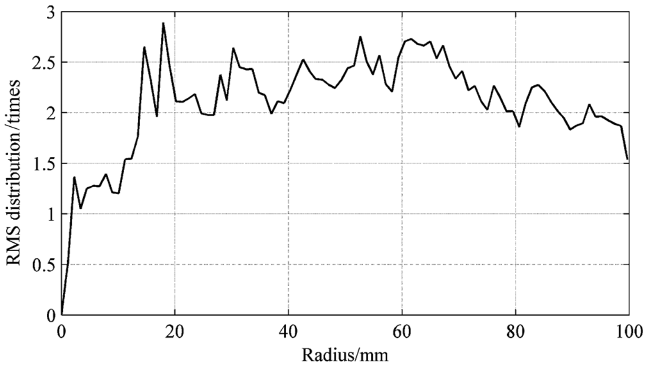

Fig. 9 RMS distribution at difference radius.

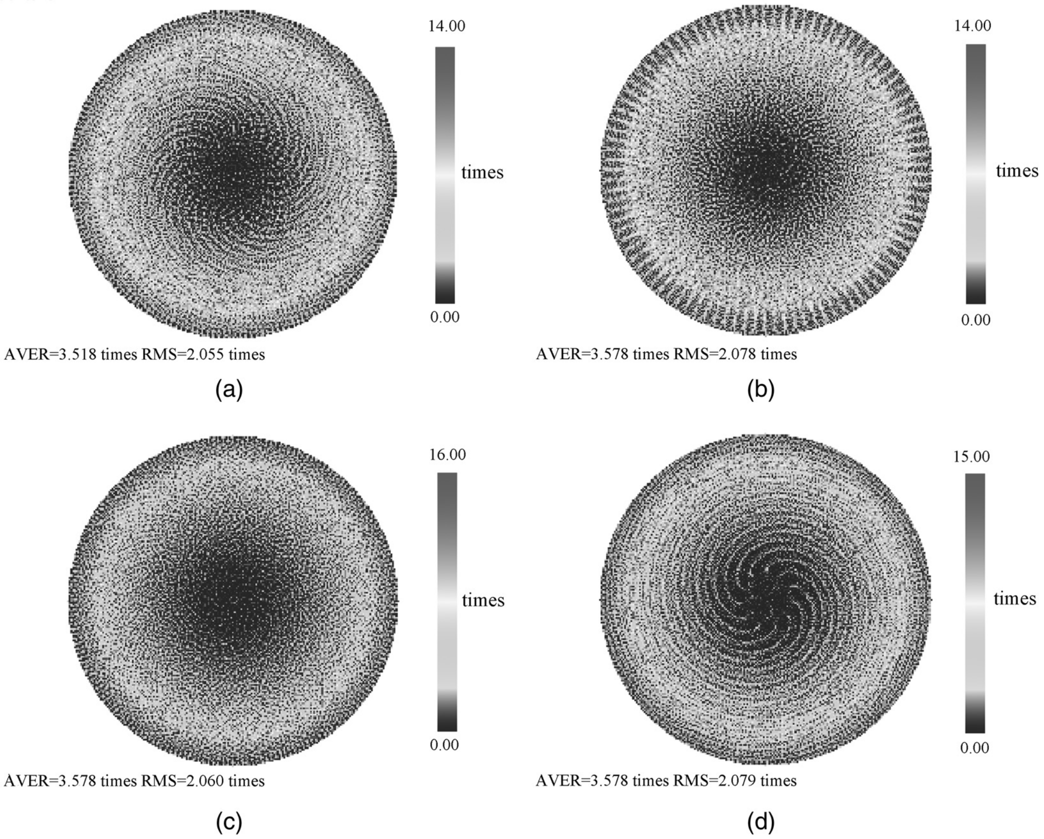

(a) (b) (c) (d)

Fig. 10 Accumulation topography at differences proportional coefficients when $\Omega = 20$: (a) $\kappa = 8.35$, (b) $\kappa = 8.71$, (c) $\kappa = 9.45$, (d) $\kappa = 9.95$.

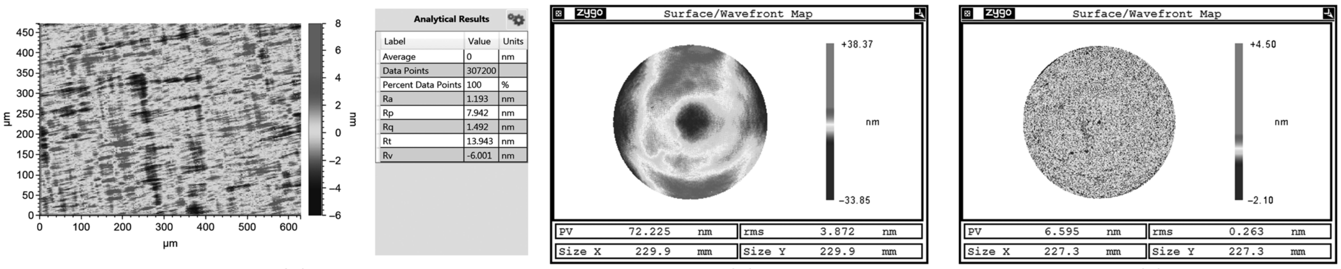

Analytical Results

Label	Value	Units
Average	0	nm
Data Points	307200	
Percent Data Points	100	%
Ra	1.193	nm
Rp	7.942	nm
Rq	1.492	nm
Rt	13.943	nm
Rv	-6.001	nm

Surface/Wavefront Map

```
PV       72.225    nm   rms      3.872     nm
Size X   229.9     mm   Size Y   229.9     mm
```

Surface/Wavefront Map

```
PV       6.595     nm   rms      0.263     nm
Size X   227.3     mm   Size Y   227.3     mm
```

(a) (b) (c)

Fig. 11 Representative results before processing: (a) surface roughness, (b) figure error, and (c) mid-frequency error (1 to 10 mm).

the average and root mean square value of the overlapping times, respectively.

As shown in Fig. 8, the accumulation figure texture, which is influenced by the revolution path, appeared in the peripheral distribution. According to the character of the accumulation figure, the RMS values of the points on the concentric rings are calculated to analyze the uniformity of the synthesis path. Figure 9 shows the RMS values distribution at different radius, which is the evaluation result of Fig. 8.

Table 1 Technology parameters.

Parameter	Value	Unit	Description
Ω	19	rpm	Angular velocity of revolution motion
ω	214	rpm	Angular velocity of the tool spinning motion
η	100	—	Controlling pitch
ρ_0	2.5	mm	Radius of constant v
l	0.8	L/min	Slurry flow
r_0	15	mm	Polishing tool radius

4.3 *Optimization of Technology Parameters*

In order to avoid the periodic texture shown in Fig. 8, the Ω and ω need to be optimized in the practical polishing process. After the revolution path is determined, the ratio of ω to Ω

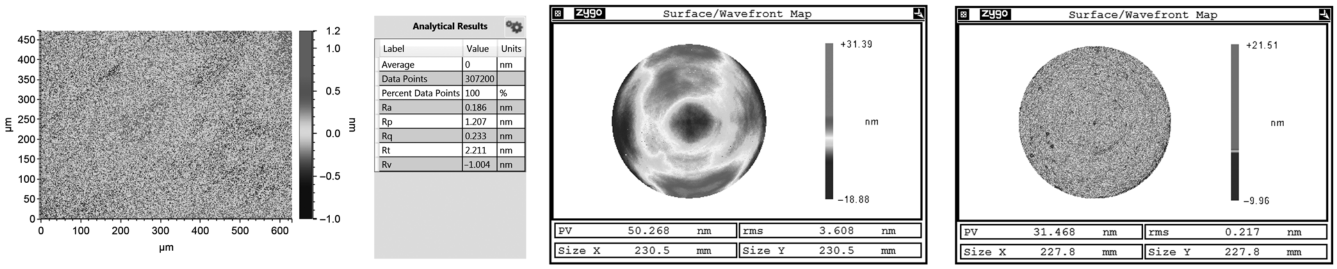

Analytical Results

Label	Value	Units
Average	0	nm
Data Points	307200	
Percent Data Points	100	%
Ra	0.186	nm
Rp	1.207	nm
Rq	0.233	nm
Rt	2.211	nm
Rv	−1.004	nm

(a)

PV	50.268	nm	rms	3.608	nm
Size X	230.5	mm	Size Y	230.5	mm

(b)

PV	31.468	nm	rms	0.217	nm
Size X	227.8	mm	Size Y	227.8	mm

(c)

Fig. 12 Representative results after processing: (a) surface roughness, (b) figure error, and (c) mid-frequency error (1 to 10 mm).

(defined as κ) is found to be one of the key factors which affect the accumulation figure texture. Thus, the optimum parameters can be obtained by searching the minimum RMS value of the whole ring series from different κ.

Figure 10 shows some accumulation texture figures under different values of κ. The RMS values become minimum when $\kappa = 9.45$. In this figure, the periodic texture is the weakest and the path distribution is the most uniform.

5 Experimental Results

To verify the correctness of the algorithm introduced in this paper, an experiment has been carried out on a ∅245 mm concave spherical lens whose radius is 214.148 mm and the material is fused silica. Before processing, the surface roughness is 1.492 nm RMS (tested by Bruker white light interferometer, 10× objective, measurement range $0.63 \times 0.47\ \text{mm}^2$, system error removed, the same as below), the figure error is 3.872 nm RMS (ZYGO GPI interferometer, 94% aperture evaluated, the same as below), and the mid-frequency error with a 1 to 10 mm bandpass filter is 0.263 nm RMS. The measurement results before processing are shown in Figs. 11(a)–11(c).

The algorithms introduced above are used to control the figure and mid-frequency errors by optimizing the processing parameters. The parameters are listed in Table 1.

After processing, the representative roughness value of this lens is reduced to $R_q = 0.233$ nm. The figure accuracy and mid-frequency error are 3.608 and 0.217 nm RMS, respectively. Figures 12(a)–12(c) show the typical measurement results. The crisscross scratches disappear and the microtopography becomes smoother after comparison between Figs. 11(a) and 12(a). The basic figure topography does not change by much, but there is a little change in the RMS value (from 3.872 nm to 3.608 nm) when comparing Figs. 11(b) and 12(b). The mid-frequency error of this lens was also suppressed by comparing Figs. 11(c) and 12(c).

This experiment indicates that the ultrasmooth surface with roughness value $R_q = 0.233$ nm was finally acquired using the AFP technology. In this processing, the figure error changed a little and the mid-frequency error is suppressed.

6 Conclusions

According to the characteristics of the AFP, a new variable pitch spiral path together with a parameter optimization algorithm is proposed in this paper. This variable pitch spiral path associated with the dwell time-solving model could control the figure accuracy in the ultrasmooth polishing. It will further suppress the mid-frequency error by evaluating the uniformity of the synthesis path and optimizing the processing parameters. An experiment was conducted on a fused silica spherical lens with an aperture of 245 mm and a radius of 214.148 mm. The experiment indicated the correctness and validity of the algorithm on full aperture processing during the AFP. More work will be done on the aspheric optical element polishing in the future.

Acknowledgments

The authors are grateful to their colleagues who cooperated to carry out the experiments and to their institution, the State Key Laboratory of Applied Optics. The research was funded by the Key Program of the Major Subject of National Science and Technology.

References

1. Z. Ma, J. Liu, and J. Wang, "Development and application of ultrasmooth optical surface polishing technology," *Laser Optoelectron. Prog.* **48**(8), 2202-1–2202-7 (2011).
2. J. M. Bennett et al., "Float polishing of optical materials," *Appl. Opt.* **26**, 696–703 (1987).
3. H. Gao, J. Cao, and X. Chen, "Float polishing subnanometer-smooth surface," *Acta Opt. Sin.* **15**(6), 824–825 (1995).
4. J.-D. Kim, "Motion analysis of powder particles in EEM using cylindrical polyurethane wheel," *Int. J. Mach. Tools Manuf.* **42**, 21–28 (2002).
5. M. Kanaoka et al., "Processing efficiency of elastic emission machining for low-thermal-expansion material," *Surf. Interface Anal.* **40**, 1002–1006 (2008).
6. Y. Mori et al., "Development of a figure correction method having spatial resolution close to 0.1 mm," *Proc. SPIE* **5193**, 105–111 (2004).
7. J. V. Wingerden, H. J. Frankena, and B. A. V. der Zwan, "Production and measurement of super polished surfaces," *Opt. Eng.* **31**, 1086–1092 (1992).
8. Z. Zhang, W. Liu, and Z. Song, "Particle size and surfactant effects on chemical mechanical polishing of glass using silica-based slurry," *Appl. Opt.* **49**, 5480–5485 (2010).
9. W. J. Choi et al., "Characterization of wet pad surface in chemical mechanical polishing (CMP) process with full-field optical coherence tomography (FF-OCT)," *Opt. Express* **19**, 11343–11350 (2011).
10. S. Wang, J. Liu, and L. Zhang, "Dual-rotor tool path generation and removal error analysis in active feed polishing," *Appl. Opt.* **52**, 5480–5485 (2013).
11. D. W. Kim, S. W. Kim, and J. H. Burge, "Non-sequential optimization technique for a computer controlled optical surfacing process using multiple tool influence functions," *Opt. Express* **17**, 21850–21866 (2009).
12. H. Fang, P. Guo, and J. Yu, "Analysis of material removal mechanism in fluid jet polishing by finite element method," *Opt. Precision Eng.* **14**(2), 218–223 (2006).
13. S. F. Soares et al., "Float-polishing process and analysis of float-polished quartz," *Appl. Opt.* **33**, 89–95 (1994).
14. Y. Namba and H. Tsuwa, "Mechanism and some applications of ultrafine finishing," *Ann. CIRP* **27**(1), 511–516 (1978).
15. F. W. Preston, "The theory and design of plate glass polishing machines," *J. Soc. Glass Technol.* **11**, 214–256 (1927).
16. Y. Dai, W. Shang, and X. Zhou, "Effection of the material of a small tool to the removal function in computer control optical polishing," *J. Natl Univ. Defense Technol.* **28**(2), 97–101 (2006).

17. H. Fang, P. Guo, and J. Yu, “Dwell function algorithm in fluid jet polishing,” *Appl. Opt.* **45**, 4291–4296 (2006).
18. Y. Zhang et al., “Analysis of dwell time algorithm based on optimization theory for computer controlled optical surfacing,” *High Power Laser Particle Beams* **23**, 3239–3244 (2011).
19. X. Peng et al., “Dwell time algorithm for MRF of axis-symmetrical aspherical parts,” *J. Natl Univ. Defense Technol.* **26**(3), 89–92 (2004).
20. C. R. Dunn and D. D. Walker, “Pseudo-random tool paths for CNC sub-aperture polishing and other applications,” *Opt. Express* **16**, 18942–18949 (2008).
21. C. Shi et al., “Analysis of polishing errors by tool paths and optimization of tool paths,” *Acta Opt. Sin.* **31**(8), 22003-1–22003-5 (2011).
22. J. D. Yang and C. L. Tian, *High Speed Lapping Technology*, National Defense Industry Press, Beijing (2003).
23. X. Zhou et al., “Correcting errors in definite area: a new method for controlling mid-spatial-frequency errors in optical surface,” *Opt. Precision Eng.* **15**(11), 1668–1673 (2007).

Jian Liu is currently an assistant professor at Changchun Institute of Optics, Fine Mechanics and Physics, Chinese Academy of Sciences. He received his BS degree from Taiyuan University of Technology in 2007 and his MS degree from Tianjin University in 2009. His research interests include advanced optical fabrication, polishing machine tool design, as well as computer-controlled optical surfacing techniques.

Shaozhi Wang is currently an assistant professor at Changchun Institute of Optics, Fine Mechanics and Physics, Chinese Academy of Sciences. He received his BS degree from Harbin Institute of Technology in 2008 and his MS degree in 2010. His research interests include advanced optical fabrication and advanced control techniques.

Chunlei Zhang is currently an assistant professor at Changchun Institute of Optics, Fine Mechanics and Physics (CIOMP), Chinese Academy of Sciences. He received his PhD from CIOMP in 2011. His research interests include advanced optical fabrication and test techniques.

Linghua Zhang is currently an assistant professor at Changchun Institute of Optics, Fine Mechanics and Physics, Chinese Academy of Sciences. She received her MS degree from Harbin Institute of Technology in 2010. Her research interests include test techniques and advanced optical fabrication.

Huanan Chen received his master’s degree from Harbin Institute of Technology in 2011. He is now an assistant professor at Changchun Institute of Optics, Fine Mechanics and Physics, Chinese Academy of Sciences. His research interests include precision mechanisms, optics applications, and opto-mechanical systems.